

# A Spectral/Spatial CBIR System for Hyperspectral Images

Miguel Angel Veganzones, *Student Member, IEEE*, and Manuel Graña, *Member, IEEE*

**Abstract**—This paper introduces a novel content-based image retrieval (CBIR) system for hyperspectral image databases using both spectral and spatial features computed following an unsupervised unmixing process which minimizes human intervention. The set of endmembers obtained from the image by an Endmember Induction Algorithm provides the image spectral features. Spatial features are computed as abundance image statistics. Both kinds of information are functionally combined into a dissimilarity measure between two hyperspectral images. This dissimilarity measure guides the search for answers to database queries. The system allows the user to retrieve hyperspectral images containing materials similar to the query image, and in a similar proportion. We provide validation results using both synthetic hyperspectral datasets and real hyperspectral data.

**Index Terms**—Content-based image retrieval (CBIR) systems, CBIR quality measures, endmember induction, hyperspectral images, image synthesis, linear unmixing.

## I. INTRODUCTION

A CONTENT-BASED image retrieval (CBIR) system [1]–[3] is able to retrieve the images stored in an image database using as image indexing values feature vectors extracted from the images by means of computer vision and digital image-processing techniques. Conventional search in image databases is performed on the basis of metadata provided by the sensor or the human interaction. Sensor metadata may include time and position data, while human metadata refer to the human interpretation of the image contents. In CBIR approaches, image metadata is automatically generated by the machine interpretation of the image contents, with minimal human intervention. Specifically, in query-by-example CBIR, the interrogation to the database is done through the presentation of a query image, and the query's answer consists of the most similar images in the database according to some similarity measure defined on the image feature space.

The increasing amount of Earth Observation data provided by hyperspectral sensors, motivates research in some technological problems raised by the sheer scale of the amount of available data. Among them, searching through these huge databases using CBIR techniques has not been properly addressed for

the case of hyperspectral images. Approaches to CBIR in remote-sensing image databases reported in the literature are focused on panchromatic images, SAR data, or low-dimensional multispectral images such as LANDSAT [4]–[6]. There are few works in the literature dealing explicitly with the spectral information to guide the search [7]–[10]. These works define the image features as the endmembers induced from the hyperspectral data by some Endmember Induction Algorithm (EIA). One inconvenience of these CBIR systems is that they can not discriminate among images with the same induced endmembers but very different spatial distributions. In this paper, we propose a spectral–spatial feature extraction process, that makes this discrimination possible, and we provide an evaluation of its effectiveness on synthetic and real hyperspectral data.

The proposed spectral–spatial CBIR system for hyperspectral imagery relies on the linear mixing formulation [11] to extract the spectral–spatial features that drive the retrieval process. We conduct experiments using two well-known EIAs, the N-FINDER [12] and the Fast Iterative Pixel Purity Index (FIPPI) [13], and a fast and light algorithm based on lattice computing, the Incremental Lattice Strong Independence Algorithm (ILSIA) [14]. We also used the Harsanyi–Farand–Chang (HFC) virtual dimensionality method [15] to estimate the number of endmembers when required, and the fully constrained least squares unmixing (FCLSU) method [16] to estimate the fractional abundances. However, hyperspectral imaging has been profited from a rapid growth in computational methods in the last years [17]. Those include a bunch of new subspace identification methods, endmember induction algorithms, and fractional abundances estimation techniques. Among them, improvements in endmember induction such as simplex-based algorithms robust to noise and highly mixed pixels [18], [19], fast implementations [20], algorithms preserving anomaly endmembers [21], [22], or algorithms taking into account the spatial information [23], [24]; new techniques for virtual dimensionality and subspace identification [25]–[29]; and robust estimation of the full-constrained fractional abundances [30]–[32] or new methods for nonlinear unmixing [33], [34]. Also, new hyperspectral representations are explored [35], and big efforts are being made to speed up hyperspectral imaging to bring it closer to a real-time process [36]. These rapid advances would contribute to enhance the performance of the proposed and future hyperspectral CBIR systems.

This paper is organized as follows. Section II provides a description of the spectral–spatial CBIR system. Section III describes the methodological issues of its validation. Section IV gives the validation results using synthetic hyperspectral images. Section V gives validation results using a real hyperspec-

Manuscript received July 20, 2011; revised November 18, 2011; accepted December 21, 2011. Date of publication March 14, 2012; date of current version May 23, 2012. The work of M. A. Veganzones was supported by the Basque Government under predoctoral grant BFI.07.225.

The authors are with the Grupo de Inteligencia Computacional, Universidad del País Vasco (UPV/EHU), Donostia, Spain (corresponding author, e-mail: miguelangel.veganzones@ehu.es).

Color versions of one or more of the figures in this paper are available online at <http://ieeexplore.ieee.org>.

Digital Object Identifier 10.1109/JSTARS.2012.2186629

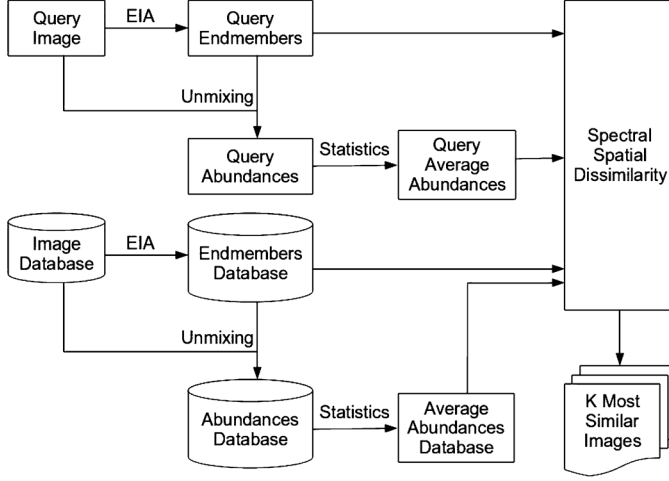


Fig. 1. Spectral-spatial CBIR system's schema.

tral dataset. Section VI gives our conclusions and directions for further work.

## II. SPECTRAL-SPATIAL CBIR SYSTEM

We first describe the spectral-spatial CBIR system's architecture, next we detail the spectral-spatial feature characterization, and the spectral-spatial dissimilarity function over which the proposed CBIR system is built.

### A. System's Architecture

Fig. 1 shows the spectral-spatial CBIR system scheme. The core of the CBIR system is the spectral-spatial dissimilarity function between two hyperspectral images by means of their spectral and spatial features. The system interacts with a feature database where the spectral-spatial features of the images are stored. These features have been previously extracted by offline application of an EIA and a spectral unmixing method using the endmembers extracted by the EIA from the image. System interrogation is done using a query example approach. First, the query example is processed to extract its spectral-spatial features and second, it is compared to the images in the database using the spectral-spatial dissimilarity measure. A ranking of the images in the database is elaborated by ascending order of dissimilarity to the query. Finally, the system returns the  $k$  images in the database corresponding to the first  $k$  ranking positions, where  $k$  is known as the query's *scope*.

### B. Spectral-Spatial Feature Extraction Process

Hyperspectral images in the database are indexed by low-level feature vectors that are extracted and stored offline. To that effect, we assume the linear mixing model, where a hyperspectral image is the result of the linear combination of the pure spectral signatures of ground components, named endmembers, with a fractional abundance matrix.

Let  $\mathbf{E} = [\mathbf{e}_1, \dots, \mathbf{e}_m]$  be the pure endmember signatures (normally corresponding to macroscopic objects in scene, such as water, soil, vegetation, and so on) where each  $\mathbf{e}_i \in \mathbb{R}^q$  is

a  $q$ -dimensional vector. Then, the hyperspectral signature  $\mathbf{r}$  at each pixel in the image is defined by the expression

$$\mathbf{r} = \mathbf{s} + \mathbf{n} = \sum_{i=1}^m \mathbf{e}_i \phi_i + \mathbf{n} \quad (1)$$

where the hyperspectral signature  $\mathbf{r}$  is formed by the sum of the pixel's signal  $\mathbf{s}$  and an independent additive noise component  $\mathbf{n}$  and  $\phi$  is the  $m$ -dimensional vector of fractional abundances at the given pixel subject to constraints:  $\phi_i \geq 0, \forall i = 1, \dots, m$ , and  $\sum_{i=1}^m \phi_i = 1$ . This equation can be extended to the full image as  $\mathbf{H} = \mathbf{E}\Phi + \boldsymbol{\eta}$ , where  $\mathbf{H}$  is the hyperspectral image,  $\Phi$  is a matrix of fractional abundances, and  $\boldsymbol{\eta}$  is independent additive noise.

We characterize a hyperspectral image  $H_\alpha$  by a tuple  $(E_\alpha, \Phi_\alpha)$ , where  $E_\alpha = \{\mathbf{e}_1^\alpha, \mathbf{e}_2^\alpha, \dots, \mathbf{e}_{m_\alpha}^\alpha\}$  is the set of  $m_\alpha$  induced endmembers from the  $\alpha$ th image, and  $\Phi_\alpha = \{\phi_1^\alpha, \phi_2^\alpha, \dots, \phi_{m_\alpha}^\alpha\}$  is the set of fractional abundance maps resulting from the unmixing process, where each  $\phi_i^\alpha$  represents the spatial distribution of the induced endmember  $\mathbf{e}_i^\alpha, i = 1, \dots, m_\alpha$ , in the image. We refer to the tuple  $(E_\alpha, \Phi_\alpha)$  as the *spectral-spatial features* of the hyperspectral image  $H_\alpha$ .

To implement this approach, an EIA is first used to induce the spectral signatures (the endmembers) of the image, and then an unmixing method calculates from the image the spatial distribution of each endmember (the fractional abundances).

### C. Spectral-Spatial Dissimilarity Measure

The spectral-spatial CBIR system of Fig. 1 uses a dissimilarity measure between the spectral-spatial features of hyperspectral images described above. The aim is to declare images sharing some of their constituent materials as similar. We detect this similarity through the similarity between image spectra and their relative abundance proportions. The spectral-spatial dissimilarity is a version of the Integrated Region Matching (IRM) dissimilarity function [37] used for region matching-based image retrieval. The overall IRM dissimilarity between two images depends on two aspects: the similarity between each region pair from the two images, and the significance of each region pair matching. To build our spectral-spatial dissimilarity measure, we establish a correspondence between IRM regions and spectral signatures. Region pair matching corresponds to the matching of pairs of spectral signatures built on the distance between each pair of the endmembers from both images. Significance corresponds to endmember average abundances.

Let  $E_\alpha = \{\mathbf{e}_1^\alpha, \mathbf{e}_2^\alpha, \dots, \mathbf{e}_{m_\alpha}^\alpha\}$  be the set of endmembers induced from the hyperspectral image  $H_\alpha$  in the database, where  $m_\alpha$  is the number of induced endmembers from the  $\alpha$ th image, and  $\bar{\Phi}_\alpha = \{\bar{\phi}_1^\alpha, \bar{\phi}_2^\alpha, \dots, \bar{\phi}_{m_\alpha}^\alpha\}$  is the normalized average abundances of  $H_\alpha$ , where  $\bar{\phi}_i^\alpha = (1)/(M) \sum_{j=1}^M (\phi_i^\alpha(j)) / (\sum_{k=1}^{m_\alpha} \phi_k^\alpha(j))$ ,  $i = 1, \dots, m_\alpha$ , where  $\phi_i^\alpha(j)$  is the  $i$ th endmember fractional abundance for a pixel  $j$ , and  $M$  the number of pixels in the image. Given two images  $H_\alpha$  and  $H_\beta$ , we first compute the spectral distance matrix  $D_{\alpha,\beta}$  as

$$D_{\alpha,\beta} = [d_{ij}, ; i = 1, \dots, m_\alpha; j = 1, \dots, m_\beta] \quad (2)$$

whose elements  $d_{ij}$  are the distances between the endmembers  $\mathbf{e}_i^\alpha, \mathbf{e}_j^\beta \in \mathbb{R}^q$  of each image. Any spectral distance function  $d : \mathbb{R}^q \times \mathbb{R}^q \rightarrow \mathbb{R}^+$  can be used, for instance, the Euclidean distance or the angular pseudo-distance (SAM) [38].

Then, we define the spectral-spatial dissimilarity measure  $s(H_\alpha, H_\beta)$  as

$$s(H_\alpha, H_\beta) = \sum_{i,j} r_{ij} d_{ij} \quad (3)$$

where  $d_{ij}$  is the spectral distance between endmembers  $\mathbf{e}_i^\alpha$  and  $\mathbf{e}_j^\beta$ , and  $r_{ij}$  is the significance associated with  $d_{ij}$ .

The formulation of the measure needs a definition for the significance matrix  $R_{\alpha,\beta} = [r_{ij}; i = 1, \dots, m_\alpha; j = 1, \dots, m_\beta]$ . We follow the *most similar highest priority* (MSHP) principle [37], making use of the normalized average abundances  $\bar{\Phi}_\alpha$  and  $\bar{\Phi}_\beta$ . The average abundances represent “significance credits” assigned to the endmember spectral distances by Algorithm 1.

---

**Algorithm 1: Significance credits assignment algorithm**

---

- 1) Set  $\mathcal{L} = \{\}$ .
  - 2) Denote  $\mathcal{M} = \{(i, j) : i = 1, \dots, m_\alpha; j = 1, \dots, m_\beta\}$ .
  - 3) Choose the minimum  $d_{ij}$  for  $(i, j) \in \mathcal{M} - \mathcal{L}$ . Label the corresponding  $(i, j)$  as  $(i', j')$ .
  - 4)  $r_{i'j'} = \min\{\bar{\phi}_{i'}^\alpha, \bar{\phi}_{j'}^\beta\}$ .
  - 5) If  $\bar{\phi}_{i'}^\alpha < \bar{\phi}_{j'}^\beta$ , set  $r_{ij'} = 0$ , for all  $j \neq j'$ ; otherwise, set  $r_{ij'} = 0$ , for all  $i \neq i'$ .
  - 6) If  $\bar{\phi}_{i'}^\alpha < \bar{\phi}_{j'}^\beta$ , set  $\bar{\phi}_{i'}^\alpha = 0$  and  $\bar{\phi}_{j'}^\beta = \bar{\phi}_{j'}^\beta - \bar{\phi}_{i'}^\alpha$ ; otherwise, set  $\bar{\phi}_{j'}^\beta = 0$  and  $\bar{\phi}_{i'}^\alpha = \bar{\phi}_{i'}^\alpha - \bar{\phi}_{j'}^\beta$ .
  - 7)  $\mathcal{L} = \mathcal{L} + \{(i', j')\}$ .
  - 8) If  $\sum_{i=1}^{m_\alpha} \bar{\phi}_i^\alpha > 0$  and  $\sum_{j=1}^{m_\beta} \bar{\phi}_j^\beta > 0$ , go to step 3; otherwise, stop.
- 

The algorithm for the assignment of significance credits starts by initializing the set of all possible endmember pairs  $\mathcal{M} = \{(i, j) : i = 1, \dots, m_\alpha; j = 1, \dots, m_\beta\}$ , where  $m_\alpha$  and  $m_\beta$  indicate the number of endmembers for images  $H_\alpha$  and  $H_\beta$ , respectively, and the set of previously selected endmember pairs,  $\mathcal{L} = \{\}$  (steps 1 and 2). In each subsequent iteration, the algorithm first selects the pair of endmembers  $(i, j) : i = 1, \dots, m_\alpha; j = 1, \dots, m_\beta$ , with minimum spectral distance,  $d_{ij}$ , from the set of available pairs,  $(i, j) \in \mathcal{M} - \mathcal{L}$  (step 3). Let  $(i', j')$  denote the selected pair. Second, the value of the minimum of the average fractional abundances is assigned as the pair's corresponding significance,  $r_{i'j'} = \min\{\bar{\phi}_{i'}^\alpha, \bar{\phi}_{j'}^\beta\}$  (step 4). Notice that the average abundances are always equal to or greater than zero. If  $\bar{\phi}_{i'}^\alpha < \bar{\phi}_{j'}^\beta$ , then the elements of significance matrix row  $i'$  are set to zero; otherwise, the elements of significance matrix column  $j'$  are set to zero (step 5). Then, the pool of significance credits is reduced. If  $\bar{\phi}_{i'}^\alpha < \bar{\phi}_{j'}^\beta$ , then set  $\bar{\phi}_{i'}^\alpha = 0$  and  $\bar{\phi}_{j'}^\beta = \bar{\phi}_{j'}^\beta - \bar{\phi}_{i'}^\alpha$ ; otherwise, set  $\bar{\phi}_{j'}^\beta = 0$  and  $\bar{\phi}_{i'}^\alpha = \bar{\phi}_{i'}^\alpha - \bar{\phi}_{j'}^\beta$  (step 6). Finally,  $(i', j')$  is added to the set of previously selected pairs,  $\mathcal{L}$  (step 7). When the stopping condition  $\sum_{i=1}^{m_\alpha} \bar{\phi}_i^\alpha = 0$  or  $\sum_{j=1}^{m_\beta} \bar{\phi}_j^\beta = 0$  is met, the algorithm ends; otherwise a new iteration starts (step 8).

### III. SPECTRAL-SPATIAL CBIR SYSTEM VALIDATION

There are two key elements of the validation process. First, the performance measures used to compare the diverse instances of the system obtained by different parametrizations. Second, the strategy followed to obtain the reference measures. Namely, how the ground truth references are obtained and used to compute the benchmarking performance measures.

#### A. CBIR Performance Measures

Evaluation metrics from information retrieval field have been adopted to evaluate CBIR systems quality. The two most used evaluation measures are *precision* and *recall* [1], [5]. Precision  $p$  is the fraction of the returned images that are relevant to the query. Recall  $q$  is the fraction of returned relevant images respect to the total number of relevant images in the database according to *a priori* knowledge. If we denote  $T$  the set of returned images and  $R$  the set of all of the images relevant to the query, then

$$p = \frac{|T \cap R|}{|T|} \quad (4)$$

$$r = \frac{|T \cap R|}{|R|}. \quad (5)$$

Precision and recall follow inverse trends when considered as functions of the scope of the query. Precision falls while recall increases as the scope increases. To evaluate the overall performance of a CBIR system, the Average Precision and Average Recall are calculated over all the query images in the database. For a query of scope  $k$ , these are defined as

$$P_k = \frac{1}{N} \sum_{\alpha=1}^N P_k(H_\alpha) \quad (6)$$

and

$$R_k = \frac{1}{N} \sum_{\alpha=1}^N R_k(H_\alpha). \quad (7)$$

The normalized rank [39] is a performance measure used to summarize system performance into a scalar value. The normalized rank for a given image ranking  $\Omega_\alpha$ , denoted as  $\text{Rank}(H_\alpha)$ , is defined as

$$\text{Rank}(H_\alpha) = \frac{1}{N N_\alpha} \left( \sum_{i=1}^{N_\alpha} \Omega_\alpha^i - \frac{N_\alpha(N_\alpha - 1)}{2} \right) \quad (8)$$

where  $N$  is the number of images in the dataset,  $N_\alpha$  is the number of relevant images for the query  $H_\alpha$ , and  $\Omega_\alpha^i$  is the rank at which the  $i$ th image is retrieved. This measure is 0 for perfect performance and approaches 1 as performance worsens, where 0.5 is equivalent to a random retrieval. The average normalized rank (ANR) for the full dataset is given by

$$\text{ANR} = \frac{1}{N} \sum_{\alpha=1}^N \text{Rank}(H_\alpha). \quad (9)$$

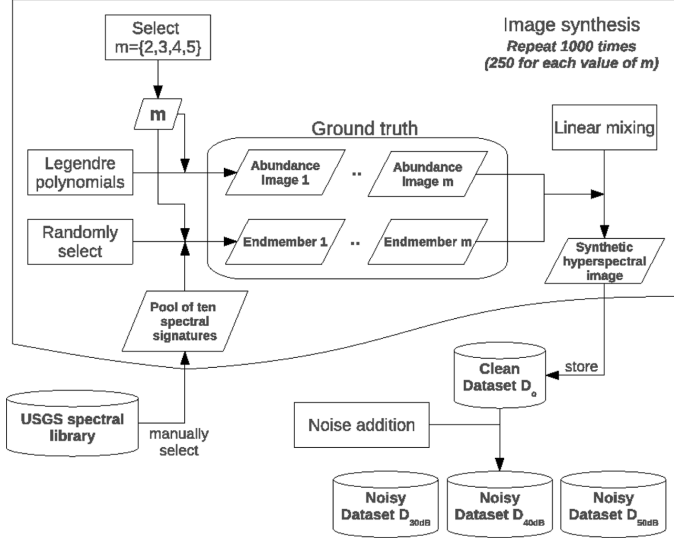


Fig. 2. Schema of the hyperspectral datasets synthesis process.

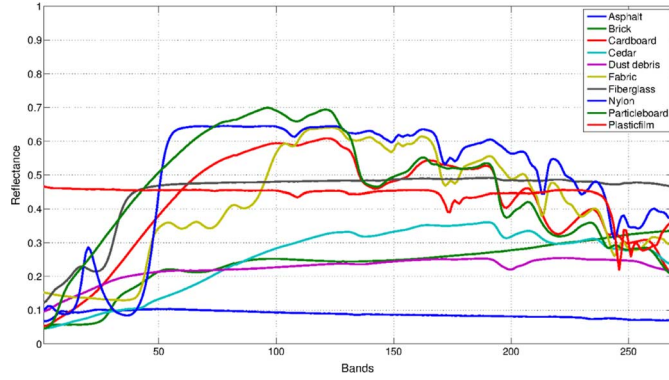


Fig. 3. Pool of endmembers selected from the USGS spectral library.

### B. Validation Methodology

We perform separate validation experiments using a synthetic dataset and real data. In both cases, we follow a similar methodology, explained below. However, each dataset serves to validate different aspects of the spectral-spatial CBIR system. We make use of a synthetic dataset to test the system robustness against changes in its internal components, that is, the selected spectral distance and methods used to extract the spectral-spatial features, as well as the system robustness against noisy data. In the experiments with real data, we test the applicability of the proposed system in a real scenario.

The general methodology followed in all of the experiments has two main phases. First, we perform offline the spectral-spatial feature extraction of the hyperspectral images in the given dataset. For each image, we apply independently either the ILSIA, the N-FINDER, or the FIPPI EIAs to induce the set of endmembers. Therefore, we have three competing spectral features of each image. A brief review of these three EIAs is given in an Appendix. ILSIA is fully automatic and do not require any input parameter. N-FINDER and FIPPI requires as input the estimation of the number of endmembers in the image,  $m$ . For the latter EIAs,  $m$  is estimated by means of the HFC virtual dimensionality method setting the false alarm rate to  $\alpha = 10^{-5}$ . The number of endmembers induced by ILSIA

and FIPPI algorithms may be different from the HFC method estimation. For each set of induced endmembers, we calculate their respective spatial fractional abundances using the FCLSU method.

In the second phase, for each hyperspectral image  $H_\alpha$  in a dataset, we calculate the dissimilarity measure of (3) between  $H_\alpha$  and each of the remaining images in the dataset. These dissimilarities are represented as a vector  $s_\alpha = [s_{\alpha 1}, \dots, s_{\alpha N}]$ , where  $N$  is the number of images in the dataset and  $s_{\alpha, \beta}$  is the dissimilarity between the images  $H_\alpha$  and  $H_\beta$ , with  $\alpha, \beta = 1, \dots, N$ . We can define the ranking of the dataset relative to the query image,  $\Omega_\alpha = [\omega_{\alpha, p} \in \{1, \dots, N\}; p = 1, \dots, N]$ , as the set of image indexes ordered according to increasing values of their corresponding entries in the dissimilarity vector  $s_\alpha$ , that is, we sort in increasing order the components of  $s_\alpha$ , and the resulting shuffled image indexes constitute  $\Omega_\alpha$ , so that  $s_{\alpha, \omega_{\alpha, p}} \leq s_{\alpha, \omega_{\alpha, p+1}}$ . The ranking  $\Omega_\alpha$  can be computed either on the ground truth information or on the induced endmembers and estimated abundances.

Finally, we estimate the spectral-spatial CBIR system performance measures, average precision, average recall, and average normalized rank as follows. For each hyperspectral image  $H_\alpha$ , a query  $Q_k(H_\alpha)$  is formulated returning the  $k$  most similar (less dissimilar) images  $H_\beta$  in the dataset relative to the image  $H_\alpha$ , where  $k$  is the scope of the query and takes values in the range  $1 \leq k \leq N$ . The set of returned images  $T_k(H_\alpha)$  and the set of relevant images  $V_k(H_\alpha)$  for a query  $Q_k(H_\alpha)$  used to calculate the CBIR performance measures can be obtained from the rankings computed from the induced endmembers and the ground truth, respectively.

## IV. VALIDATION USING SYNTHETIC DATASETS

We use a collection of synthetic hyperspectral images to test the robustness of the proposed spectral-spatial CBIR system to variations on the selected spectral distance, and the applied end-member induction algorithms. We also test the influence in the system performance of random noise added to the synthetic images. Here we start by describing how we construct the synthetic hyperspectral images. Next, we comment on the specific methodological details, and, finally, we give the results of the experiments.

### A. Synthetic Dataset

The synthetic hyperspectral images are generated as linear mixtures of a set of spectra (the groundtruth endmembers) according to synthesized fractional abundance coefficients. The generation of the abundance coefficients is a spatial process performed independently for each desired endmember, which does not ensure for each pixel in the image the normalization properties required by the linear mixing model. To ensure them, the resulting collection of abundance images for all endmembers are processed imposing normalization conditions independently for each pixel.

Fig. 2 shows a flow diagram of the synthesis process of an images. First we select the number of endmembers  $m \in \{2, 3, 4, 5\}$ . This number controls the number of synthetic groundtruth abundance images that will be generated using Legendre polynomials, and the number of endmember spectral

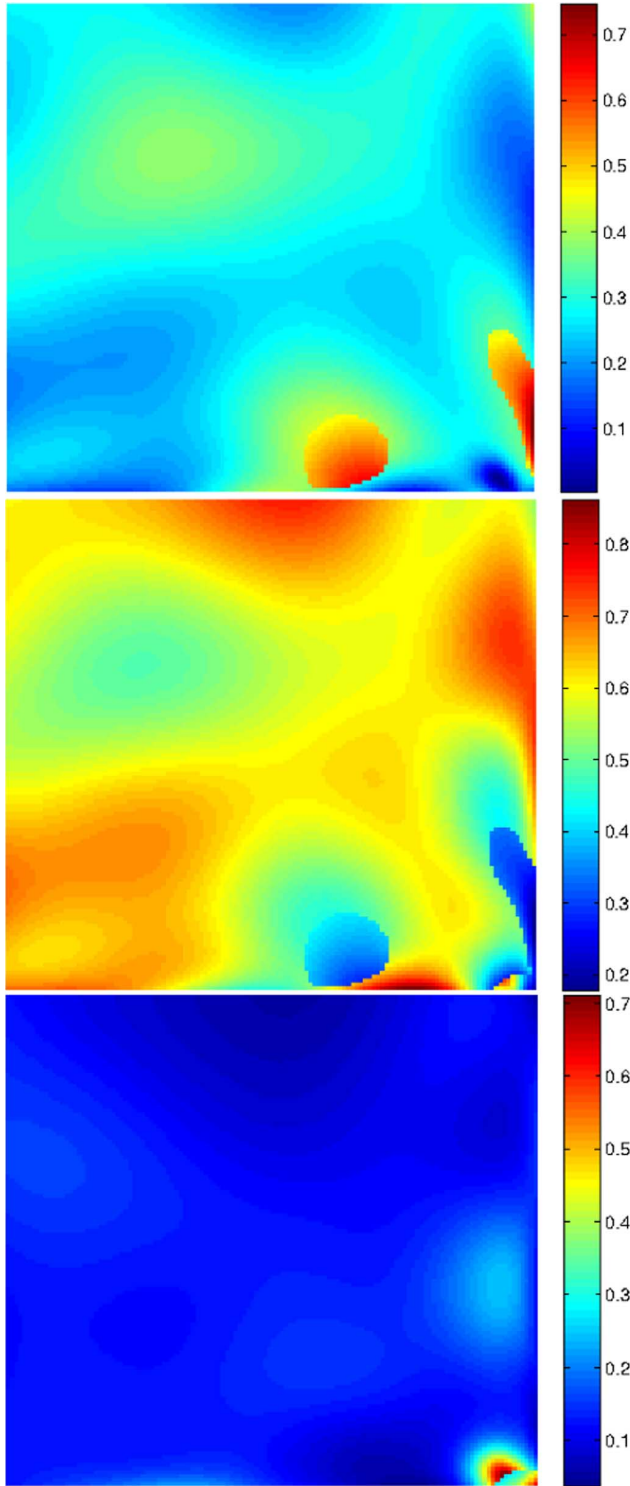


Fig. 4. Instance of synthetic fractional abundance images generated using random Legendre polynomials.

signatures that will be selected from the pool of ten endmembers obtained from the USGS library. The abundance images are used to produce the linear combinations of endmembers at each pixel to obtain the resulting image. The hyperspectral image is then stored as clean image, and subjected to noise corruption to obtain the noisy datasets.

TABLE I  
SAMPLE MEAN AND SAMPLE STANDARD DEVIATION OF THE NUMBER OF ENDMEMBERS INDUCED FROM THE SYNTHETIC DATASETS RELATIVE TO THE EIA AND THE NUMBER OF ENDMEMBERS,  $m$ , USED FOR THE IMAGE SYNTHESIS.  
(a)  $D^{(64)}$  AND (b)  $D^{(128)}$

	$D_o^{(64)}$	$D_{30dB}^{(64)}$	$D_{40dB}^{(64)}$	$D_{50dB}^{(64)}$
ILSIA ( $m = 2$ )	$2.03 \pm 0.17$	$2.98 \pm 0.61$	$3.54 \pm 1.01$	$4.03 \pm 1.27$
ILSIA ( $m = 3$ )	$2.02 \pm 0.13$	$3.13 \pm 0.65$	$3.57 \pm 1.04$	$3.88 \pm 1.31$
ILSIA ( $m = 4$ )	$2.06 \pm 0.23$	$3.13 \pm 0.77$	$3.55 \pm 1.01$	$3.66 \pm 1.24$
ILSIA ( $m = 5$ )	$2.08 \pm 0.28$	$3.17 \pm 0.75$	$3.66 \pm 1.23$	$3.52 \pm 1.29$
N-FINDR ( $m = 2$ )	$2.00 \pm 0.06$	$1.98 \pm 0.14$	$2.00 \pm 0.06$	$2.00 \pm 0.06$
N-FINDR ( $m = 3$ )	$2.88 \pm 0.33$	$2.74 \pm 0.48$	$2.88 \pm 0.33$	$2.88 \pm 0.33$
N-FINDR ( $m = 4$ )	$3.69 \pm 0.52$	$3.10 \pm 0.78$	$3.61 \pm 0.60$	$3.68 \pm 0.52$
N-FINDR ( $m = 5$ )	$4.44 \pm 0.70$	$3.42 \pm 0.91$	$4.13 \pm 0.83$	$4.40 \pm 0.73$
FIPPI( $m = 2$ )	$2.18 \pm 0.62$	$3.14 \pm 0.68$	$3.23 \pm 0.63$	$3.15 \pm 0.65$
FIPPI ( $m = 3$ )	$2.32 \pm 0.73$	$3.85 \pm 1.00$	$3.92 \pm 0.93$	$3.75 \pm 1.03$
FIPPI( $m = 4$ )	$2.26 \pm 0.72$	$4.13 \pm 1.23$	$4.25 \pm 1.17$	$4.06 \pm 1.25$
FIPPI( $m = 5$ )	$2.38 \pm 0.78$	$4.32 \pm 1.30$	$4.42 \pm 1.39$	$4.20 \pm 1.36$

(a)

	$D_o^{(128)}$	$D_{30dB}^{(128)}$	$D_{40dB}^{(128)}$	$D_{50dB}^{(128)}$
ILSIA ( $m = 2$ )	$2.06 \pm 0.23$	$3.36 \pm 0.73$	$4.02 \pm 1.21$	$4.83 \pm 1.70$
ILSIA ( $m = 3$ )	$2.02 \pm 0.15$	$3.54 \pm 0.91$	$4.11 \pm 1.35$	$4.51 \pm 1.49$
ILSIA ( $m = 4$ )	$2.09 \pm 0.29$	$3.52 \pm 0.80$	$4.32 \pm 1.35$	$4.66 \pm 1.76$
ILSIA ( $m = 5$ )	$2.10 \pm 0.30$	$3.72 \pm 0.95$	$4.20 \pm 1.41$	$4.23 \pm 1.69$
N-FINDR ( $m = 2$ )	$2.00 \pm 0.00$	$2.00 \pm 0.00$	$2.00 \pm 0.00$	$2.00 \pm 0.00$
N-FINDR ( $m = 3$ )	$2.94 \pm 0.24$	$2.84 \pm 0.39$	$2.93 \pm 0.26$	$2.94 \pm 0.24$
N-FINDR ( $m = 4$ )	$3.84 \pm 0.37$	$3.49 \pm 0.63$	$3.80 \pm 0.41$	$3.84 \pm 0.37$
N-FINDR ( $m = 5$ )	$4.63 \pm 0.58$	$3.69 \pm 0.82$	$4.36 \pm 0.77$	$4.60 \pm 0.59$
FIPPI( $m = 2$ )	$2.17 \pm 0.59$	$3.20 \pm 0.57$	$3.20 \pm 0.55$	$3.17 \pm 0.57$
FIPPI ( $m = 3$ )	$2.21 \pm 0.58$	$4.00 \pm 0.95$	$3.95 \pm 0.94$	$3.83 \pm 0.96$
FIPPI( $m = 4$ )	$2.27 \pm 0.68$	$4.58 \pm 1.26$	$4.45 \pm 1.31$	$4.21 \pm 1.26$
FIPPI( $m = 5$ )	$2.43 \pm 0.81$	$4.64 \pm 1.31$	$4.83 \pm 1.42$	$4.23 \pm 1.33$

(b)

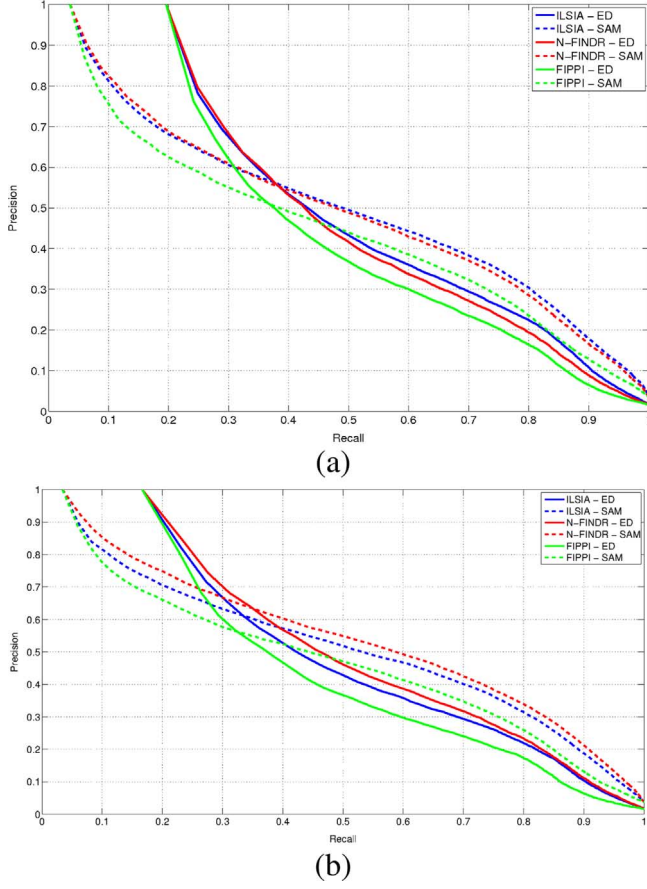
Fig. 3 shows the pool of ground-truth endmembers used for the hyperspectral image synthesis. The ten spectral signatures have been manually selected from the USGS spectral library<sup>1</sup> so they all present distinct absorption patterns. The synthetic groundtruth multidimensional fractional abundance images are generated in a two-step procedure. First, we simulate the abundance images corresponding to each endmember as 2-D product of 1-D Legendre polynomials with randomly generated parameters. Second, to ensure that there are regions of almost pure endmembers, for each pixel we select the abundance coefficient with the greatest value, normalizing the remaining coefficients to ensure that the pixel's abundance coefficients sum up to one. Fig. 4 gives an instance of synthetic fractional abundance images generated using random Legendre polynomials to build a hyperspectral image composed of three endmembers.

We have synthesized two sets of 1000 hyperspectral images, each set having a specific domain spatial size. The one denoted  $D^{(64)}$  contains  $64 \times 64$  pixel images. The second denoted  $D^{(128)}$  contains images of size  $128 \times 128$  pixels. All of the synthesized hyperspectral images have 269 spectral bands per pixel. Each synthetic image is built with a number of ground-truth endmembers,  $m \in \{2, 3, 4, 5\}$ , randomly selected from the pool of available ground-truth endmembers. For the experiments in this paper, we have generated 250 images of each number of ground-truth endmembers for each image size.

In addition to  $D^{(64)}$  and  $D^{(128)}$  datasets, hereafter named as the clean datasets, six more datasets have been built by adding random Gaussian noise to each of the clean dataset images, resulting in noise images with signal-to-noise ratios (SNRs) 30,

<sup>1</sup>[Online]. Available: <http://speclab.cr.usgs.gov/spectral-lib.html>




 Fig. 5. Precision-recall curves for  $D_o$  synthetic datasets. (a)  $D_o^{(64)}$ . (b)  $D_o^{(128)}$ .

40, and 50 dB. We denote the clean dataset as  $D_o$ , and the noisy datasets as  $D_{30 \text{ dB}}$ ,  $D_{40 \text{ dB}}$ , and  $D_{50 \text{ dB}}$ . Thereby, we have in total eight synthetic hyperspectral datasets:  $D_o^{(64)}$ ,  $D_{30 \text{ dB}}^{(64)}$ ,  $D_{40 \text{ dB}}^{(64)}$ ,  $D_{50 \text{ dB}}^{(64)}$ ,  $D_o^{(128)}$ ,  $D_{30 \text{ dB}}^{(128)}$ ,  $D_{40 \text{ dB}}^{(128)}$ , and  $D_{50 \text{ dB}}^{(128)}$ .

### B. Methodology

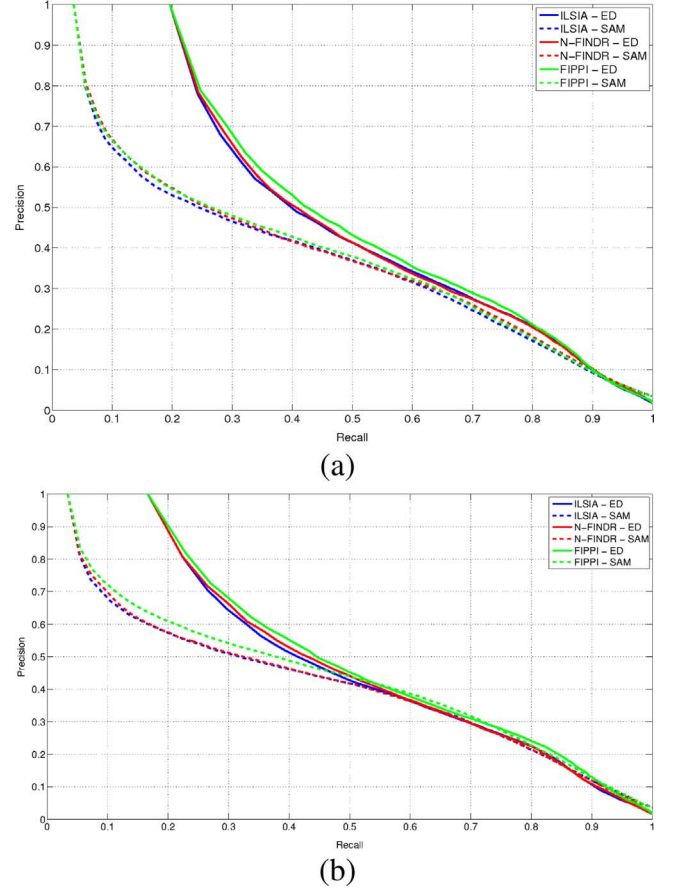
We have performed independent experiments<sup>2</sup> over each of the eight hyperspectral synthetic datasets, following the methodology explained in Section III-B. Let us distinguish between  $\mathbf{s}_\alpha^{\text{GT}}$ , the vector of dissimilarities computed using the known ground truth endmembers and fractional abundances used to synthesize the images, and  $\mathbf{s}_\alpha^{\text{IND}}$ , the vector of dissimilarities computed using the endmembers induced by one of the EIAs (either ILSIA, N-FINDER, or FIPPI) and their estimated abundances. We distinguish as well rankings  $\Omega_\alpha^{\text{GT}}$  and  $\Omega_\alpha^{\text{IND}}$  corresponding to the ground truth and induced dissimilarities, respectively.

The set of returned images  $T_k(H_\alpha)$  and the set of relevant images  $V_k(H_\alpha)$  for a query  $Q_k(H_\alpha)$  are defined as follows:

$$T_k(H_\alpha) = \Omega_{\alpha,k}^{\text{IND}} = \left[ \omega_{\alpha,p}^{\text{IND}} \text{ s.t. } s_{\alpha,\omega_{\alpha,p}^{\text{IND}}} \leq s_{\alpha,\omega_{\alpha,k}^{\text{IND}}} \right] \quad (10)$$

$$V_k(H_\alpha) = \Omega_\alpha^{\text{GT}} = \left[ \omega_{\alpha,p}^{\text{GT}} \text{ s.t. } s_{\alpha,\omega_{\alpha,p}^{\text{GT}}} \leq t \right] \quad (11)$$

<sup>2</sup>The MATLAB code for the hyperspectral image synthesis and endmember induction is publicly available at: <http://www.ehu.es/ccwintco/index.php/GIC-source-code-free-libre>


 Fig. 6. Precision-recall curves for  $D_{30 \text{ dB}}$  synthetic datasets. (a)  $D_{30 \text{ dB}}^{(64)}$ . (b)  $D_{30 \text{ dB}}^{(128)}$ .

where  $t = \bar{s}_\alpha^{\text{GT}} - 2\sigma_{\mathbf{s}_\alpha^{\text{GT}}}$ , and  $\bar{s}_\alpha^{\text{GT}}$  and  $\sigma_{\mathbf{s}_\alpha^{\text{GT}}}$  are, respectively, the mean and standard deviation of  $\mathbf{s}_\alpha^{\text{GT}}$ . This definition allows for the inclusion in the query's answer of images whose dissimilarity is equal to the maximum one, thus allowing that the cardinality of both returned and relevant sets may be bigger than  $k$ . Now  $T_k(H_\alpha)$  and  $V_k(H_\alpha)$  can be used to calculate the average precision and recall measures of the system, as well as the average normalized rank.

### C. Performance Results

Table I shows the average and standard deviation number of endmembers induced from the different EIAs for the  $D^{(64)}$  and  $D^{(128)}$  datasets. We have estimated the induced endmember values for the clean and noisy datasets in four separated groups, corresponding to the number  $m$  of ground truth endmembers used for the image synthesis. We can see that the number of endmembers induced by the N-FINDER algorithm, corresponding to the number of endmembers estimated by HFC method, is close to the actual number of endmembers in the image even in noisy datasets. The FIPPI algorithm, which uses HFC estimation as an initial value, finally induces a lower number of endmembers, and it is more sensitive to noise. The ILSIA algorithm, which does not require to *a priori* know the number of endmembers in the image, underestimates the number of actual endmembers and it is also sensible to noise conditions.

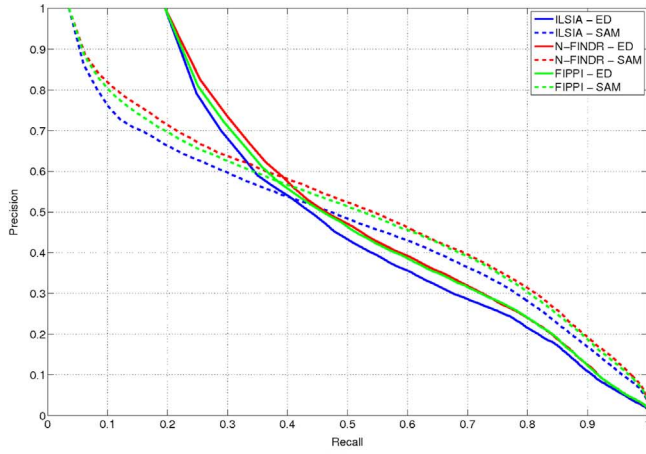
TABLE II  
ANR RESULTS FOR SYNTHETIC DATASETS. (a)  $D^{(64)}$ . (b)  $D^{(128)}$

Dataset	Averaged Normalized Rank (ANR)					
	ILSIA		N-FINDR		FIPPI	
	ED	SAM	ED	SAM	ED	SAM
$D_o^{(64)}$	<b>0.043</b>	0.053	0.050	0.058	0.064	0.074
$D_{30dB}^{(64)}$	0.045	0.101	<b>0.043</b>	0.097	<b>0.043</b>	0.099
$D_{40dB}^{(64)}$	0.042	0.057	<b>0.036</b>	0.048	0.037	0.052
$D_{50dB}^{(64)}$	0.042	0.053	<b>0.038</b>	0.045	0.041	0.051

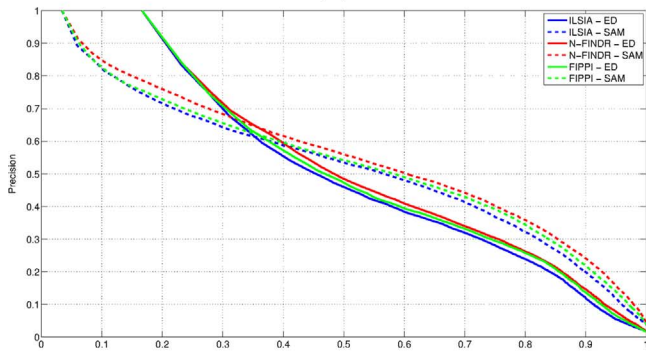
(a)

Dataset	Averaged Normalized Rank (ANR)					
	ILSIA		N-FINDR		FIPPI	
	ED	SAM	ED	SAM	ED	SAM
$D_o^{(128)}$	0.047	0.057	<b>0.044</b>	0.050	0.068	0.077
$D_{30dB}^{(128)}$	0.044	0.086	0.044	0.088	<b>0.038</b>	0.082
$D_{40dB}^{(128)}$	0.044	0.056	<b>0.035</b>	0.043	0.039	0.049
$D_{50dB}^{(128)}$	0.043	0.052	<b>0.033</b>	0.038	0.040	0.047

(b)



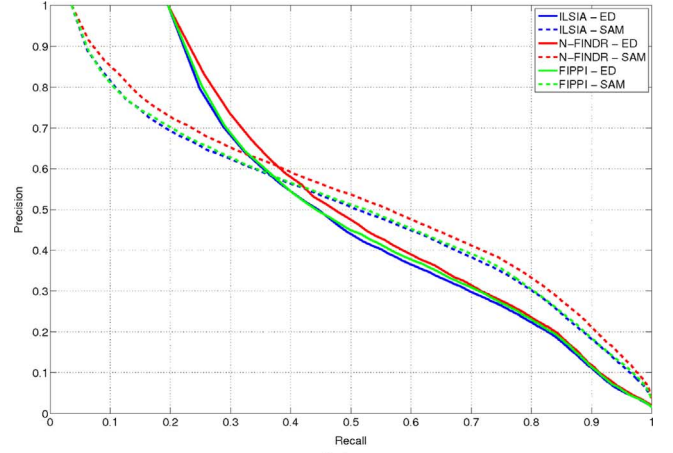
(a)



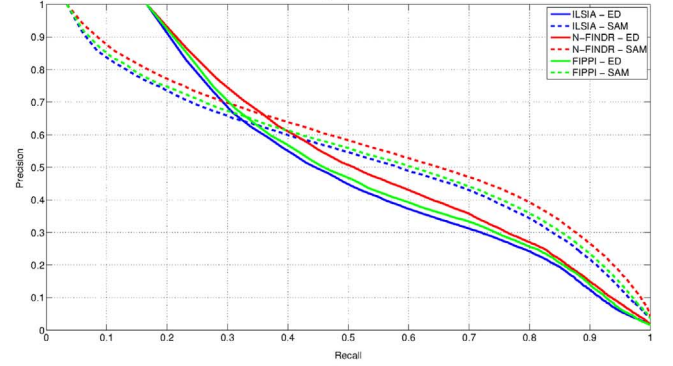
(b)

Fig. 7. Precision-recall curves for  $D_{40dB}$  synthetic datasets. (a)  $D_{40dB}^{(64)}$ . (b)  $D_{40dB}^{(128)}$ .

Figs. 5–8 show the plots of the precision-recall curves for the noise free dataset and the 30-, 40-, and 50-dB datasets, respectively. It can be appreciated that, for low levels of noise, the performance is similar to the noise-free case. In general, the plots show a rather high insensitivity to the choice of EIA and individual endmember spectral distance, because corresponding curves are not very different, except in the limit of low recall



(a)



(b)

Fig. 8. Precision-recall curves for  $D_{50dB}$  synthetic datasets. (a)  $D_{50dB}^{(64)}$ . (b)  $D_{50dB}^{(128)}$ .

values where a clear sensitivity to the individual endmember distance is made apparent. The light better performance of N-FINDR can be explained by the greater number of endmembers induced by this algorithm compared to ILSIA and FIPPI algorithms. However, the little differences between algorithms performance suggests that the fewer endmembers induced by ILSIA and FIPPI contain the most relevant information for image comparison. The Euclidean distance systematically gets better results than the SAM distance, giving higher precision at the same recall value. Increasing recall value range reverses the picture, so that the SAM distance improves systematically over the Euclidean distance in the noise free case. One effect of the noise is the cancellation of this effect. For the highest noise (30 dB), the SAM never improves the Euclidean distance. Other effect of the noise is the attenuation of the effect of the EIA chosen. In the noise free data set, the ILSIA and N-FINDR show a small improvement on the FIPPI, however, these relations change according to the noise level, being attenuated at the highest noise level.

The differences between the performance results on datasets  $D^{(64)}$  and  $D^{(128)}$  are almost negligible showing that the spatial size by itself, without an increasing in the number of distinct materials, does not modify the proposed Spectral/Spatial CBIR system performance.

Table II gives the Averaged Normalized Rank values obtained. The results confirm the conclusions from the figures.



Fig. 9. Hyperspectral scene by HyMAP sensor capturing the DLR facilities in Oberpfaffenhofen and its surroundings.

The SAM distance is most affected by noise, showing the worse results for the noisiest data. The Euclidean distance is much more robust relative to noise. Comparing the effect of the EIA chosen, the ILSIA gives the best result in the noise free data, and the differences between algorithms are attenuated for the noisiest data.

TABLE III  
SAMPLE MEAN AND SAMPLE STANDARD DEVIATION OF THE NUMBER OF ENDMEMBERS INDUCED FROM THE REAL HyMAP CATEGORIES RELATIVE TO THE EIA

	ILSIA	N-FINDR	FIPPI
Forests	$3.85 \pm 1.16$	$7.31 \pm 1.26$	$5.64 \pm 1.31$
Fields	$2.99 \pm 0.80$	$6.16 \pm 1.57$	$4.42 \pm 1.28$
Urban Areas	$2.75 \pm 0.61$	$4.33 \pm 1.09$	$3.50 \pm 1.06$
Mixed	$2.98 \pm 0.80$	$5.83 \pm 1.71$	$4.26 \pm 1.50$
Others	$2.77 \pm 0.60$	$5.31 \pm 1.66$	$3.94 \pm 1.35$

## V. VALIDATION USING REAL DATA

Here, we test the proposed spectral–spatial CBIR system over a dataset of real hyperspectral images to validate the system usage in a real scenario. We also compare it with the system proposed in [8], hereafter named as Plaza’s CBIR system. We first introduce the hyperspectral dataset used in the experiments, we follow explaining the specific methodological aspects of the experiments, and, finally, we give the results.

### A. HyMAP Dataset

The hyperspectral HyMAP data was made available from HyVista Corporation and German Aerospace Center’s (DLR) optical Airborne Remote Sensing and Calibration Facility service.<sup>3</sup> The sensed scene corresponds to the radiance captured by the sensor in a flight line over the facilities of the DLR center in Oberpfaffenhofen (Germany) and its surroundings, mostly fields, forests and small towns. Fig. 9 shows the scene captured by the HyMAP sensor. The data cube has 2878 lines, 512 samples, and 125 bands, and the pixel values are represented by 2-bytes signed integers.

We cut the scene in patches of  $64 \times 64$  pixels size for a total of 360 patches forming the hyperspectral database used in the experiments. We grouped the patches by visual inspection in five rough categories. The three main categories are “Forests,” “Fields,” and “Urban Areas,” representing patches that mostly belong to one of these categories. A “Mixed” category was defined for those patches that presented more than one of the three main categories, being not any of them dominant. Finally, we defined a fifth category, “Others,” for those patches that did not represent any of the above or that were not easily categorized by visual inspection. The number of patches per category are: 1) Forests: 39; 2) Fields: 160; 3) Urban Areas: 24; 4) Mixed: 102; and 5) Others: 35.

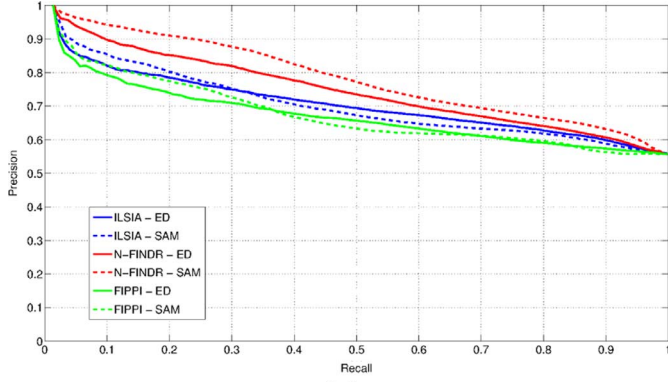
### B. Methodology

We perform three experiments to validate the use of the proposed spectral–spatial CBIR system in a real-life scenario. In the first experiment, we tested the system using the patches belonging to the three main categories: Forests, Fields, and Urban Areas. In the second experiment, we added patches from the fourth category: Mixed. Finally, in third experiment, we used the full patches database.

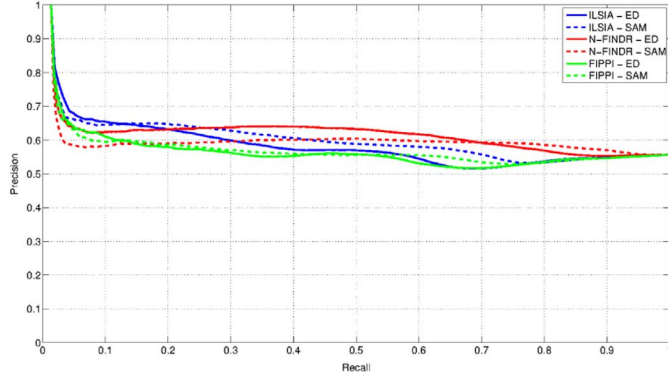
Let us denote  $s_{\alpha}^{\text{IND}}$  as the vector of dissimilarities computed using the endmembers induced by one of the EIAs (either ILSIA, N-FINDER or FIPPI) and  $\Omega_{\alpha}^{\text{IND}}$  to their respective

<sup>3</sup>[Online]. Available: <http://www.OpAIRS.aero>





(a)



(b)

Fig. 10. Precision-recall curves for HyMAP experiment 1. (a) Spectral-spatial CBIR. (b) Plaza's CBIR.

TABLE IV  
ANR RESULTS FOR HYMAP EXPERIMENT 1.  
(a) SPECTRAL-SPATIAL CBIR. (b) PLAZA'S CBIR.

Category	Averaged Normalized Rank (ANR)					
	ILSIA		N-FINDR		FIPPI	
	ED	SAM	ED	SAM	ED	SAM
Forests	0.115	0.069	0.083	<b>0.023</b>	0.143	0.082
Fields	0.093	0.109	0.090	<b>0.079</b>	0.119	0.128
Urban Areas	0.334	0.250	0.152	<b>0.010</b>	0.255	0.220
Average	0.181	0.143	0.108	<b>0.068</b>	0.172	0.143

(a)

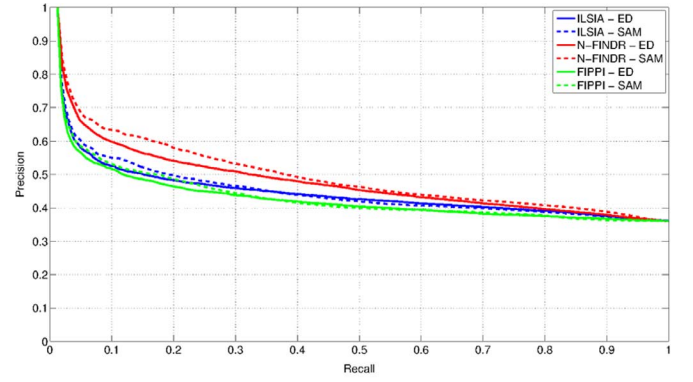
Category	Averaged Normalized Rank (ANR)					
	ILSIA		N-FINDR		FIPPI	
	ED	SAM	ED	SAM	ED	SAM
Forests	0.140	0.192	0.197	0.301	<b>0.136</b>	0.191
Fields	0.170	0.154	0.136	<b>0.133</b>	0.178	0.171
Urban Areas	0.374	0.318	0.316	0.298	0.322	<b>0.268</b>
Average	0.228	0.221	0.216	0.244	0.212	<b>0.210</b>

(b)

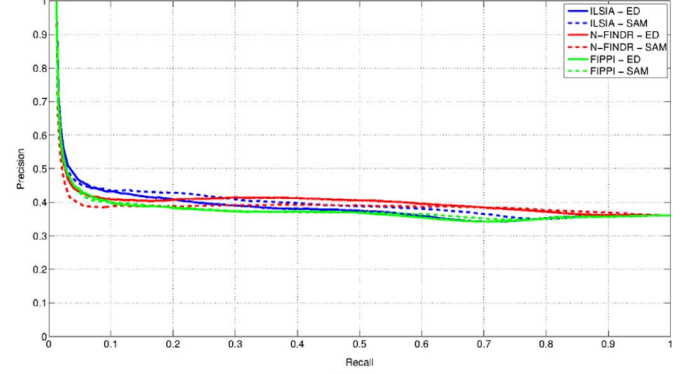
rankings. The groundtruth is given by the *a priori* categorization made by visual inspection, and the set of relevant images is composed in a different way to previous experiments using synthetic data. Given a query  $Q_k(H_\alpha)$ , the set of returned images  $T_k(H_\alpha)$  and the set of relevant images  $V_k(H_\alpha)$  are defined as follows:

$$T_k(H_\alpha) = \Omega_{\alpha,k}^{\text{IND}} = \left[ \omega_{\alpha,p}^{\text{IND}} \text{ s.t. } s_{\alpha,\omega_{\alpha,p}^{\text{IND}}} \leq s_{\alpha,\omega_{\alpha,k}^{\text{IND}}} \right] \quad (12)$$

$$V_k(H_\alpha) = \Omega_{\alpha}^{\text{GT}} = [\beta \text{ s.t. } \mathcal{C}(\beta) = \mathcal{C}(\alpha)] \quad (13)$$



(a)



(b)

Fig. 11. Precision-recall curves for HyMAP experiment 2. (a) Spectral-spatial CBIR. (b) Plaza's CBIR.

TABLE V  
ANR RESULTS FOR HYMAP EXPERIMENT 2.  
(a) SPECTRAL-SPATIAL CBIR. (b) PLAZA'S CBIR.

Category	Averaged Normalized Rank (ANR)					
	ILSIA		N-FINDR		FIPPI	
	ED	SAM	ED	SAM	ED	SAM
Forests	0.146	0.097	0.115	<b>0.054</b>	0.169	0.113
Fields	0.194	0.213	0.187	<b>0.180</b>	0.219	0.227
Urban Areas	0.338	0.255	0.156	<b>0.108</b>	0.253	0.220
Mixed	0.356	<b>0.340</b>	0.352	0.348	0.364	0.359
Average	0.259	0.226	0.203	<b>0.173</b>	0.251	0.230

(a)

Category	Averaged Normalized Rank (ANR)					
	ILSIA		N-FINDR		FIPPI	
	ED	SAM	ED	SAM	ED	SAM
Forests	0.176	0.230	0.242	0.329	<b>0.160</b>	0.214
Fields	0.275	0.261	0.239	<b>0.236</b>	0.283	0.278
Urban Areas	0.405	0.350	0.335	0.324	0.345	<b>0.287</b>
Mixed	0.337	<b>0.320</b>	0.333	0.341	0.341	0.338
Average	0.298	0.290	0.287	0.307	0.282	<b>0.279</b>

(b)

where  $\mathcal{C}(\gamma)$  indicates the category to which the patch  $H_\gamma$  belongs. This way, the relevant set for a query patch  $H_\alpha$  is formed for all those patches belonging to its same category  $\mathcal{C}(\alpha)$ . Now  $T_k(H_\alpha)$  and  $V_k(H_\alpha)$  can be used to calculate the average precision and recall measures of the system, as well as the average normalized rank.

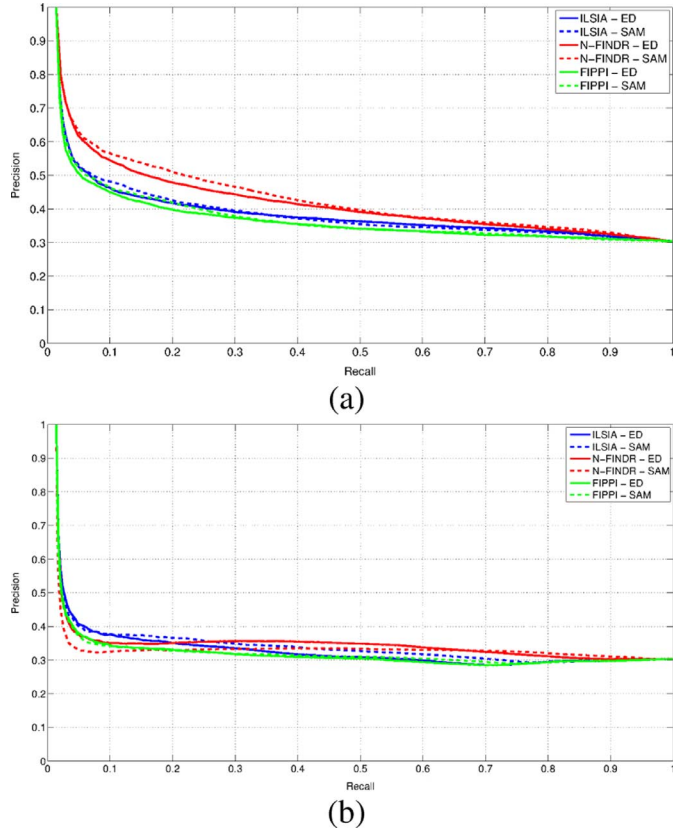


Fig. 12. Precision-recall curves for HyMAP experiment 3. (a) Spectral-spatial CBIR. (b) Plaza's CBIR.

TABLE VI  
ANR RESULTS FOR HYMAP EXPERIMENT 3.  
(a) SPECTRAL-SPATIAL CBIR. (b) PLAZA'S CBIR.

Category	Averaged Normalized Rank (ANR)					
	ILSIA		N-FINDR		FIPPI	
	ED	SAM	ED	SAM	ED	SAM
Forests	0.139	0.095	0.109	<b>0.051</b>	0.166	0.113
Fields	0.211	0.228	0.197	<b>0.196</b>	0.236	0.242
Urban Areas	0.336	0.261	0.155	<b>0.119</b>	0.250	0.224
Mixed	0.360	<b>0.347</b>	0.352	0.356	0.372	0.368
Other	0.460	0.466	0.455	<b>0.404</b>	0.482	0.463
Average	0.301	0.280	0.254	<b>0.225</b>	0.301	0.282

(a)

Category	Averaged Normalized Rank (ANR)					
	ILSIA		N-FINDR		FIPPI	
	ED	SAM	ED	SAM	ED	SAM
Forests	0.179	0.233	0.240	0.326	<b>0.162</b>	0.217
Fields	0.304	0.287	0.260	<b>0.256</b>	0.313	0.304
Urban Areas	0.419	0.361	0.341	0.334	0.357	<b>0.295</b>
Mixed	0.360	<b>0.341</b>	0.348	0.354	0.366	0.359
Other	<b>0.352</b>	0.378	0.403	0.412	0.357	0.387
Average	0.323	0.320	0.319	0.336	<b>0.311</b>	0.313

(b)

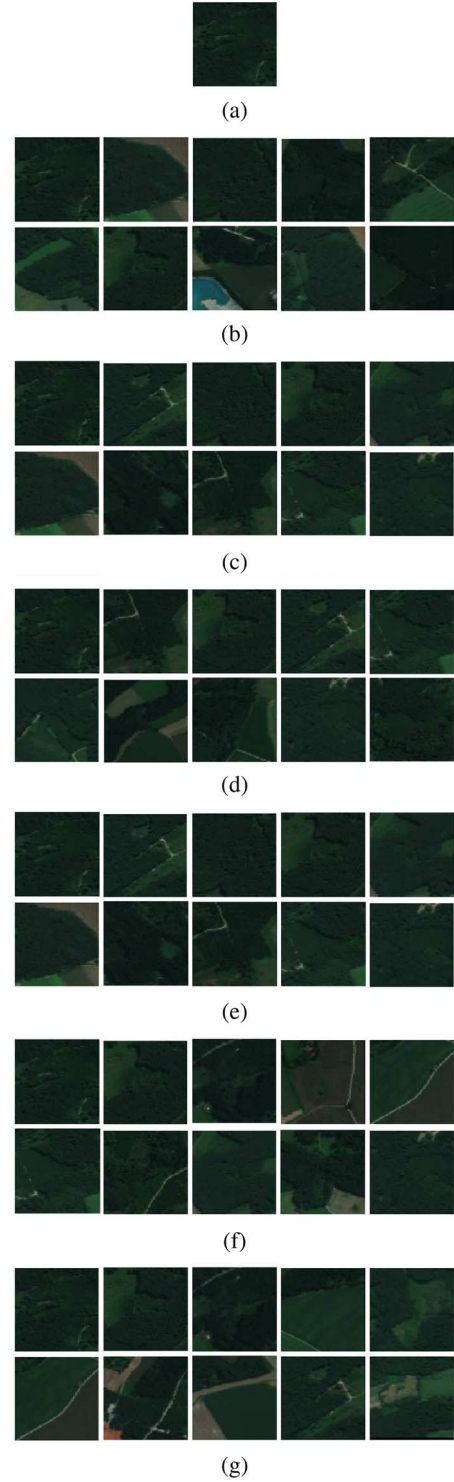


Fig. 13. Images retrieved by the proposed spectral-spatial CBIR system for a Forest query example from experiment 3. (a) Forest query example. (b) ILSIA + ED. (c) ILSIA + SAM. (d) N-FINDR + ED. (e) N-FINDR + SAM. (f) FIPPI + ED. (g) FIPPI + SAM.

### C. Performance Results

Table III shows the average number of endmembers induced by the three EIAs for each of the five categories. The results coincide with the values obtained over the synthetic data in the sense that N-FINDR algorithm induces the most number of endmembers and ILSIA algorithm the least. We can see also that the

average number of endmembers induced for Forests and Fields patches is slightly greater than for the other categories.

Fig. 10 shows the precision-recall curve for the first experiment, with varying EIA and endmember distance. Surprisingly, for the proposed spectral-spatial CBIR system the best result correspond to the SAM distance, when using the N-FINDR

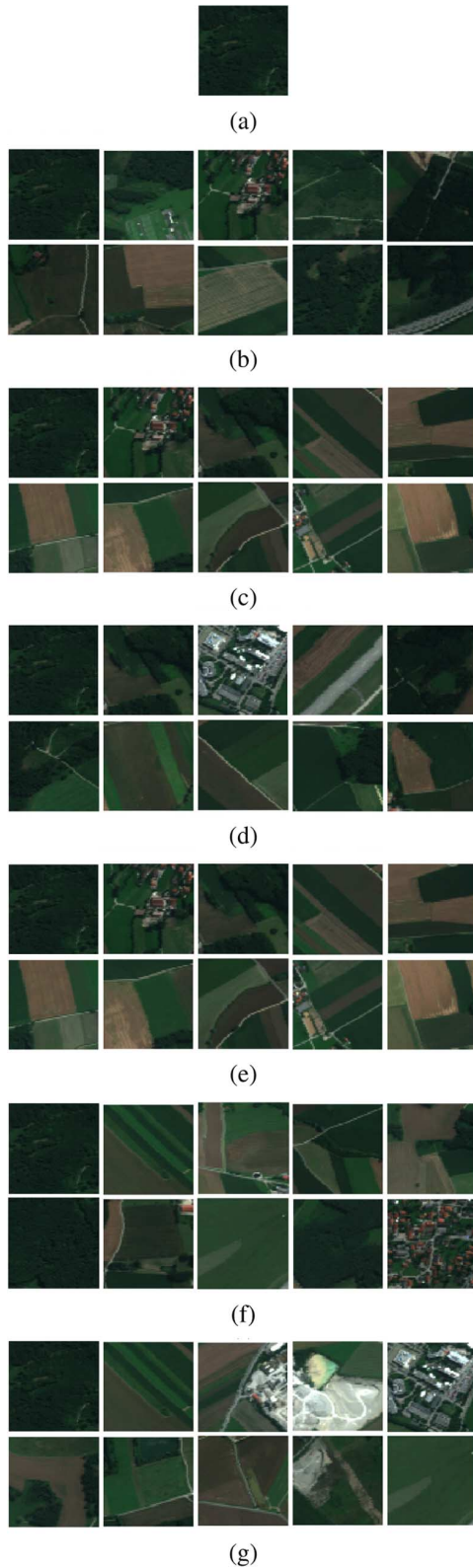


Fig. 14. Images retrieved by Plaza's CBIR system for a Forest query example from experiment 3. (a) Forest query example. (b) ILSIA + ED. (c) ILSIA + SAM. (d) N-FINDR + ED. (e) N-FINDR + SAM. (f) FIPPI + ED. (g) FIPPI + SAM.

endmember induction. For low recall values, the differences between algorithms and distances are negligible. In all combinations, the precision-recall curves are very high, showing that

the approach is feasible for real-life applications. In Table IV, we have the ANR results for the first experiment. Notice that most values when computing the SAM among endmembers induced by N-FINDR are below 0.1. These results strengthen the evidence from synthetic datasets experiments that N-FINDR performs slightly better because it induces more endmembers than the competing EIAs, but that the little differences in performance suggest that those additional endmembers contains redundant information. However, that is not the case for the Urban Areas category, where N-FINDR performs much better combined with the SAM distance. These could be because urban areas spectral signatures vary significantly more in amplitude than forests and fields due to illumination conditions. Thus, N-FINDR successes in finding endmembers containing this spectral information and SAM distance performs better than Euclidean distance to assess this amplitude difference.

Adding new categories, the performance of the system degrades gracefully, as shown in Figs. 11 and 12, maintaining high precision for low recall values. The ANR results in Tables V and VI still provide the best results for SAM distance. This must be due to the magnitude normalization performed by the SAM that removes some illumination effects that are stronger for the Euclidean distance. In all cases, the nonhomogeneous categories, such as Urban Area, Mixed, and Other, are the most difficult to retrieve, and the inclusion of new categories does not help to improve retrieval figures. Figs. 13 and 14 shows examples of a Forest category patch for both, the proposed spectral-spatial CBIR system and the Plaza's CBIR system, respectively.

Comparing with the competing Plaza's CBIR system, the proposed spectral-spatial CBIR system severely improves it, achieving the former a better performance only for the Mixed category in experiment 3.

## VI. CONCLUSION

This paper introduces a spatial-spectral CBIR system, providing validation results on synthetic and real hyperspectral data. The source code for the synthetic data is free and available via the research group's site. To validate our approach, we have followed a rigorous methodological framework using both synthetic and real datasets. The results on the synthetic datasets demonstrate the system robustness against noise and changes in the choice of endmember induction algorithm and endmember distances. The results on the real data confirm the usefulness of the proposed system. Further comparison with other CBIR systems based on other features would reinforce this conclusion.

Further research efforts will be addressed to the definition of a convenient user interaction for relevance feedback implementations based on the one-class SVM and/or similar classification approaches. There is also a big effort in hyperspectral community to develop new endmember induction algorithms, subspace identification techniques, and unmixing methods both linear and non-linear. In this paper, we focused on well-established endmember induction algorithms, using the HFC virtual dimensionality method when required, and in a full-constrained linear unmixing. However, the use of new techniques improving the extraction of spectral-spatial features should improve the overall performance of the proposed spectral-spatial CBIR system.



## ACKNOWLEDGMENT

The authors would like to thank Dr. M. Bachmann, DLR, for his support.

## REFERENCES

- [1] A. Smeulders, M. Worring, S. Santini, A. Gupta, and R. Jain, "Content-based image retrieval at the end of the early years," *IEEE Trans. Pattern Anal. Mach. Intell.*, vol. 22, no. 12, pp. 1349–1380, Dec. 2000.
- [2] M. S. Lew, N. Sebe, C. Djeraba, and R. Jain, "Content-based multimedia information retrieval: State of the art and challenges," *ACM Trans. Multimedia Comput. Commun. Appl.*, vol. 2, no. 1, pp. 1–19, 2006.
- [3] Y. Liu, D. Zhang, G. Lu, and W. Ma, "A survey of content-based image retrieval with high-level semantics," *Pattern Recognit.*, vol. 40, pp. 262–282, Jan. 2007.
- [4] M. Datcu, H. Daschiel, A. Pelizzari, M. Quartulli, A. Galoppo, A. Colapicchioni, M. Pastori, K. Seidel, P. Marchetti, and S. D'Elia, "Information mining in remote sensing image archives: System concepts," *IEEE Trans. Geosci. Remote Sens.*, vol. 41, no. 12, pp. 2923–2936, Dec. 2003.
- [5] H. Daschiel and M. Datcu, "Information mining in remote sensing image archives: System evaluation," *IEEE Trans. Geosci. Remote Sens.*, vol. 43, no. 1, pp. 188–199, Jan. 2005.
- [6] M. Datcu and K. Seidel, "Human-centered concepts for exploration and understanding of earth observation images," *IEEE Trans. Geosci. Remote Sens.*, vol. 43, no. 3, pp. 601–609, Mar. 2005.
- [7] J. Maldonado, D. Vicente, M. Veganzones, and M. Graña, "Spectral indexing for hyperspectral image CBIR," in *Proc. ESA-EUSC Image Information Mining for Security Intell. Conf.*, Madrid, Spain, 2006.
- [8] A. Plaza, J. Plaza, A. Paz, and S. Blazquez, "Parallel CBIR system for efficient hyperspectral image retrieval from heterogeneous networks of workstations," in *Proc. Int. Symp. Symbolic Numeric Algorithms Sci. Computing*, Sep. 2007, pp. 285–291.
- [9] M. A. Veganzones, J. O. Maldonado, and M. Graña, "On Content-Based image retrieval systems for hyperspectral remote sensing images," in *Computational Intelligence for Remote Sensing*. Berlin, Germany: Springer, 2008, vol. 133, pp. 125–144.
- [10] M. Graña, M. A. Veganzones, and J. Gallego, "An endmember-based distance for content based hyperspectral image retrieval," *Pattern Recognit.*, submitted for publication.
- [11] N. Keshava and J. F. Mustard, "Spectral unmixing," *IEEE Signal Process. Mag.*, vol. 19, no. 1, pp. 44–57, Jan. 2002.
- [12] M. E. Winter, M. R. Descour, and S. S. Shen, "N-FINDR: An algorithm for fast autonomous spectral end-member determination in hyperspectral data," *Proc. IEEE*, vol. 3753, pp. 266–275, Oct. 1999.
- [13] C. Chang and A. Plaza, "A fast iterative algorithm for implementation of pixel purity index," *IEEE Geosci. Remote Sens. Lett.*, vol. 3, no. 1, pp. 63–67, Jan. 2006.
- [14] M. Graña, D. Chyzyk, M. Garcia-Sebastian, and C. Hernandez, "Lattice independent component analysis for functional magnetic resonance imaging," *Inf. Sci.*, vol. 181, pp. 1910–1928, May 2011.
- [15] C. Chang and Q. Du, "Estimation of number of spectrally distinct signal sources in hyperspectral imagery," *IEEE Trans. Geosci. Remote Sens.*, vol. 42, no. 3, pp. 608–619, 2004.
- [16] C. L. Lawson, *Solving Least Squares Problems*. Englewood Cliffs, NJ: Prentice-Hall, Jun. 1974.
- [17] A. Plaza, J. A. Benediktsson, J. W. Boardman, J. Brazile, L. Bruzzone, G. Camps-Valls, J. Chanussot, M. Fauvel, P. Gamba, A. Gualtieri, M. Marconcini, J. C. Tilton, and G. Trianni, "Recent advances in techniques for hyperspectral image processing," *Remote Sens. Environ.*, vol. 113, no. Supplement 1, pp. S110–S122, Sep. 2009.
- [18] T. Chan, W. Ma, A. Ambikapathi, and C. Chi, "A simplex volume maximization framework for hyperspectral endmember extraction," *IEEE Trans. Geosci. Remote Sens.*, vol. 49, no. 11, pp. 4177–4193, Nov. 2011.
- [19] A. Ambikapathi, T. Chan, W. Ma, and C. Chi, "Chance-Constrained robust minimum-volume enclosing simplex algorithm for hyperspectral unmixing," *IEEE Trans. Geosci. Remote Sens.*, vol. 49, no. 11, pp. 4194–4209, Nov. 2011.
- [20] W. Xiong, C. Chang, C. Wu, K. Kalpakis, and H. M. Chen, "Fast algorithms to implement N-FINDR for hyperspectral endmember extraction," *IEEE J. Sel. Topics Appl. Earth Observations Remote Sens.*, vol. 4, no. 3, pp. 545–564, Sep. 2011.
- [21] H. Li and L. Zhang, "A hybrid automatic endmember extraction algorithm based on a local window," *IEEE Trans. Geosci. Remote Sens.*, vol. 49, no. 11, pp. 4223–4238, Nov. 2011.
- [22] O. Duran and M. Petrou, "Robust endmember extraction in the presence of anomalies," *IEEE Trans. Geosci. Remote Sens.*, vol. 49, no. 6, pp. 1986–1996, Jun. 2011.
- [23] D. R. Thompson, L. Mandrake, M. S. Gilmore, and R. Castano, "Super-pixel endmember detection," *IEEE Trans. Geosci. Remote Sens.*, vol. 48, no. 11, pp. 4023–4033, Nov. 2010.
- [24] S. Mei, M. He, Y. Zhang, Z. Wang, and D. Feng, "Improving spatial-spectral endmember extraction in the presence of anomalous ground objects," *IEEE Trans. Geosci. Remote Sens.*, vol. 49, no. 11, pp. 4210–4222, Nov. 2011.
- [25] J. M. Bioucas-Dias and J. M. Nascimento, "Hyperspectral subspace identification," *IEEE Trans. Geosci. Remote Sens.*, vol. 46, pp. 2435–2445, Aug. 2008.
- [26] C. Chang, W. Xiong, W. Liu, M. Chang, C. Wu, and C. C. Chen, "Linear spectral mixture analysis based approaches to estimation of virtual dimensionality in hyperspectral imagery," *IEEE Trans. Geosci. Remote Sens.*, vol. 48, no. 11, pp. 3960–3979, Nov. 2010.
- [27] O. Eches, N. Dobigeon, and J. Y. Tourneret, "Estimating the number of endmembers in hyperspectral images using the normal compositional model and a hierarchical bayesian algorithm," *IEEE J. Sel. Topics Signal Process.*, vol. 4, no. 3, pp. 582–591, Jun. 2010.
- [28] N. Acito, M. Diani, and G. Corsini, "Hyperspectral signal subspace identification in the presence of rare signal components," *IEEE Trans. Geosci. Remote Sens.*, vol. 48, no. 4, pp. 1940–1954, Apr. 2010.
- [29] P. Bajorski, "Second moment linear dimensionality as an alternative to virtual dimensionality," *IEEE Trans. Geosci. Remote Sens.*, vol. 49, no. 2, pp. 672–678, Feb. 2011.
- [30] F. Schmidt, A. Schmidt, E. Treguier, M. Guiheneuf, S. Moussaoui, and N. Dobigeon, "Implementation strategies for hyperspectral unmixing using Bayesian source separation," *IEEE Trans. Geosci. Remote Sens.*, vol. 48, no. 11, pp. 4003–4013, Nov. 2010.
- [31] J. L. Silvan and L. Wang, "Fully constrained linear spectral unmixing: Analytic solution using fuzzy sets," *IEEE Trans. Geosci. Remote Sens.*, vol. 48, no. 11, pp. 3992–4002, Nov. 2010.
- [32] R. Heylen, D. Burazerovic, and P. Scheunders, "Fully constrained least squares spectral unmixing by simplex projection," *IEEE Trans. Geosci. Remote Sens.*, vol. 49, no. 11, pp. 4112–4122, Nov. 2011.
- [33] A. Halimi, Y. Altmann, N. Dobigeon, and J. Tourneret, "Nonlinear unmixing of hyperspectral images using a generalized bilinear model," *IEEE Trans. Geosci. Remote Sens.*, vol. 49, no. 11, pp. 4153–4162, Nov. 2011.
- [34] R. Heylen, D. Burazerovic, and P. Scheunders, "Non-linear spectral unmixing by geodesic simplex volume maximization," *IEEE J. Sel. Topics Signal Process.*, vol. 5, no. 3, pp. 534–542, Jun. 2011.
- [35] S. Valero, P. Salembier, and J. Chanussot, "New hyperspectral data representation using binary partition tree," in *Proc. IEEE Int. Geosci. Remote Sens. Symp.*, Jul. 2010, pp. 80–83, IEEE.
- [36] A. Plaza, Q. Du, Y. Chang, and R. L. King, "High performance computing for hyperspectral remote sensing," *IEEE J. Sel. Topics Appl. Earth Observations Remote Sens.*, vol. 4, no. 3, pp. 528–544, Sep. 2011.
- [37] J. Li, J. Z. Wang, and G. Wiederhold, "IRM: Integrated region matching for image retrieval," in *Proc. 8th ACM Int. Conf. Multimedia*, Marina del Rey, CA, 2000, pp. 147–156.
- [38] C. Chang, *Hyperspectral Imaging: Techniques for Spectral Detection and Classification*, 1st ed. Berlin, Germany: Springer, Jul. 2003.
- [39] H. Muller, W. Muller, D. M. Squire, S. Marchand-Maillet, and T. Pun, "Performance evaluation in content-based image retrieval: Overview and proposals," *Pattern Recognit. Lett.*, vol. 22, pp. 593–601, Apr. 2001.



**Miguel Angel Veganzones** (S'08) received the M.Sc. degree in computer science from Universidad del Pais Vasco (UPV/EHU), Donostia, Spain, in 2005, where he is currently working toward the Ph.D. degree at the Computational Intelligence Group.

His research interest are in computational intelligence methods for remote sensing images.





**Manuel Graña Romay** (M'94) received the M.Sc. and Ph.D. degrees from Universidad del País Vasco (UPV/EHU), Donostia, Spain, in 1982 and 1989, respectively, both in computer science.

His current position is a Full Profesor (Catedrático de Universidad) with the Computer Science and Artificial Intelligence Department of the Universidad del País Vasco (UPV/EHU). He is the head of the Computational Intelligence Group (Grupo de Inteligencia Computacional). His current research interests are in applications of computational intelligence to multi-

component robotic systems, specifically linked multicomponent robotic systems, medical image in the neurosciences, multimodal human computer interaction, remote sensing image processing, content based image retrieval, lattice computing, semantic modelling, data processing, classification, and data mining.